

Near-infrared fluorescence molecular imaging of amyloid beta species and monitoring therapy in animal models of Alzheimer's disease

Xueli Zhang^{a,b,c,1}, Yanli Tian^{a,d,1}, Can Zhang^e, Xiaoyu Tian^f, Alana W. Ross^a, Robert D. Moir^e, Hongbin Sun^b, Rudolph E. Tanzi^e, Anna Moore^{a,2}, and Chongzhao Ran^{a,2}

^aMolecular Imaging Laboratory, Massachusetts General Hospital/Massachusetts Institute of Technology/Harvard Medical School Athinoula A. Martinos Center for Biomedical Imaging, Department of Radiology, Massachusetts General Hospital/Harvard Medical School, Charlestown, MA 02129; ^bSchool of Pharmacy, China Pharmaceutical University, Nanjing 210009, People's Republic of China; ^cDepartment of Pharmacy, ZhongDa Hospital, Southeast University, Nanjing 210009, People's Republic of China; ^dDepartment of Parasitology, Zhongshan School of Medicine, Sun Yat-Sen University, Guangzhou 510080, People's Republic of China; ^eGenetics and Aging Research Unit, Department of Neurology, Massachusetts General Hospital, Charlestown, MA 02129; and ^fCenter for Drug Discovery, Northeastern University, Boston MA 02115

Edited by Gregory A. Petsko, Weill Cornell Medical College, New York, NY, and approved July 1, 2015 (received for review March 18, 2015)

Near-infrared fluorescence (NIRF) molecular imaging has been widely applied to monitoring therapy of cancer and other diseases in preclinical studies; however, this technology has not been applied successfully to monitoring therapy for Alzheimer's disease (AD). Although several NIRF probes for detecting amyloid beta (A β) species of AD have been reported, none of these probes has been used to monitor changes of A β s during therapy. In this article, we demonstrated that CRANAD-3, a curcumin analog, is capable of detecting both soluble and insoluble A β species. In vivo imaging showed that the NIRF signal of CRANAD-3 from 4-mo-old transgenic AD (APP/PS1) mice was 2.29-fold higher than that from age-matched wild-type mice, indicating that CRANAD-3 is capable of detecting early molecular pathology. To verify the feasibility of CRANAD-3 for monitoring therapy, we first used the fast A β -lowering drug LY2811376, a well-characterized beta-amyloid cleaving enzyme-1 inhibitor, to treat APP/PS1 mice. Imaging data suggested that CRANAD-3 could monitor the decrease in A β s after drug treatment. To validate the imaging capacity of CRANAD-3 further, we used it to monitor the therapeutic effect of CRANAD-17, a curcumin analog for inhibition of A β cross-linking. The imaging data indicated that the fluorescence signal in the CRANAD-17-treated group was significantly lower than that in the control group, and the result correlated with ELISA analysis of brain extraction and A β plaque counting. It was the first time, to our knowledge, that NIRF was used to monitor AD therapy, and we believe that our imaging technology has the potential to have a high impact on AD drug development.

Alzheimer's | amyloid | imaging | fluorescence | curcumin

Alzheimer's disease (AD) has been considered incurable, because none of the clinically tested drugs have shown significant effectiveness (1–4). Therefore, seeking effective therapeutics and imaging probes capable of assisting drug development is highly desirable. The amyloid hypothesis, in which various A β species are believed to be neurotoxic and one of the leading causes of AD, has been considered controversial in recent years because of the failures of amyloid beta (A β)-based drug development (1, 3, 5–8). However, no compelling data can prove that this hypothesis is wrong (2, 5), and no other theories indicate a clear path for AD drug development (4). Thus the amyloid hypothesis is still an important framework for AD drug development (1–5, 9–14). Additionally, Kim and colleagues (15) recently reported that a 3D cell-culture model of human neural cells could recapture AD pathology. In this study, their finding that the accumulation of A β s could drive tau pathology provided strong support for the amyloid hypothesis (15).

It is well known that A β species, including soluble monomers, dimers, oligomers, and insoluble fibrils/aggregates and plaques,

play a central role in the neuropathology of AD (2, 5). Initially, it was thought that insoluble deposits/plaques formed by the A β peptides in an AD brain cause neurodegeneration. However, studies have shown that soluble dimeric and oligomeric A β species are more neurotoxic than insoluble deposits (16–21). Furthermore, it has been shown that soluble and insoluble species coexist during disease progression. The initial stage of pathology is represented by an excessive accumulation of A β monomers resulting from imbalanced A β clearance (22, 23). The early predominance of soluble species gradually shifts with the progression of AD to a majority of insoluble species (24, 25). Therefore imaging probes capable of detecting both soluble and insoluble A β s are needed to monitor the full spectrum of amyloidosis pathology in AD.

Thus far, three A β PET tracers have been approved by the Food and Drug Administration (FDA) for clinical applications. However, they are not approved for positive diagnosis of AD; rather, they are recommended for excluding the likelihood of AD. The fundamental limitation of these three tracers and others under development is that they bind primarily to insoluble A β s, not the more toxic soluble A β s (26–32). Clearly, work remains to be done

Significance

Drug development for Alzheimer's disease (AD) has been largely unsuccessful to date. Although numerous agents are reportedly effective in vitro, only an inadequate number of them have been tested in vivo, partially because of the lack of reliable and cost-efficient imaging methods to monitor their in vivo therapeutic effectiveness. Several amyloid beta (A β)-specific PET tracers have been used for clinical studies. However, their application for monitoring drug treatment in small animals is limited. Near-infrared fluorescence (NIRF) molecular imaging is a cheap, easy-to-use, and widely available technology for small animal studies. In this report we demonstrate, for the first time to our knowledge, that NIRF imaging can be used to monitor the loading changes of A β s in an AD mouse model.

Author contributions: X.Z., Y.T., A.M., and C.R. designed research; X.Z., Y.T., C.Z., X.T., A.W.R., and C.R. performed research; C.Z., R.D.M., and C.R. contributed new reagents/analytic tools; X.Z., Y.T., C.Z., X.T., H.S., A.M., and C.R. analyzed data; and X.Z., Y.T., R.D.M., H.S., R.E.T., A.M., and C.R. wrote the paper.

The authors declare no conflict of interest.

This article is a PNAS Direct Submission.

Freely available online through the PNAS open access option.

¹X.Z. and Y.T. contributed equally to this work.

²To whom correspondence may be addressed. Email: amoore@helix.mgh.harvard.edu or cran@nmr.mgh.harvard.edu.

This article contains supporting information online at www.pnas.org/lookup/suppl/doi:10.1073/pnas.1505420112/-DCSupplemental.

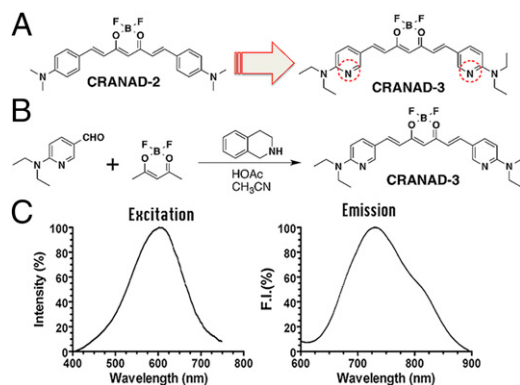


Fig. 1. Design and synthesis of CRANAD-3. (A) The design of CRANAD-3 is based on CRANAD-2. (B) Synthetic route for CRANAD-3. (C) The excitation and emission spectra of CRANAD-3 (250 nM in PBS, pH 7.4).

in developing imaging probes based on A β s, and imaging probes capable of diagnosing AD positively are undeniably needed.

Numerous agents reportedly are capable of inhibiting the generation and aggregation of A β s in vitro; however, only few have been tested in vivo. Partially, this lack of testing arises from the lack of reliable imaging methods that can monitor the agents' therapeutic effectiveness in vivo. PET tracers, such as ^{11}C -Pittsburgh compound B (^{11}C -PiB) and ^{18}F -AV-45, recently have been adapted to evaluate the efficacy of experimental AD drugs in clinical trials (33). However, they are rarely used to monitor drug treatment in small animals (30–32), likely because of the insensitivity of the tracers for A β species [particularly for soluble species (34–36)], complicated experimental procedures and data analysis in small animals, the high cost of PET probe synthesis and scanning, and the use of radioactive material. Therefore, a great demand for imaging agents that could be used in preclinical drug development to monitor therapeutic effectiveness in small animals remains unmet.

Because of its low cost, simple operation, and easy data analysis, near infrared fluorescence (NIRF) imaging is generally more suitable than PET imaging for animal studies. Several NIRF probes for insoluble A β s have been reported (37–45). It has been almost 10 y since the first report of NIRF imaging of A β s by Hintersteiner et al. in 2005 (41). However, to the best of our knowledge, successful application of NIRF probes for monitoring therapeutic efficacy has not yet been reported. Our group recently has designed asymmetrical CRANAD-58 to match the hydrophobic (LVFF) and hydrophilic (HHQK) segments of A β peptides and demonstrated its applicability for the detection of both insoluble and soluble A β s in vitro and in vivo (46). In this report, CRANAD-3 was designed to enhance the interaction with A β s by replacing the phenyl rings of curcumin with pyridyls to introduce potential hydrogen bonds. Additionally, we demonstrated, for the first time to our knowledge, that the curcumin analog CRANAD-3

could be used as an NIRF imaging probe to monitor the A β -lowering effectiveness of therapeutics.

Results

Design and Synthesis of CRANAD-3. In our previous studies, we showed that CRANAD-2, a curcumin-based NIRF imaging probe, can differentiate between 19-mo-old wild-type and transgenic mice by in vivo NIRF imaging (47). CRANAD-2 could be considered a “smart” probe because it displayed a significant increase in fluorescence intensity, an emission blue shift, a lifetime change, and quantum yield improvement upon interacting with insoluble A β aggregates (47). However, we found that CRANAD-2 was not able to detect soluble A β species (46).

Because CRANAD-2 showed a significant fluorescence response to A β aggregates/fibrils but not to monomeric A β , we speculated that the interaction between monomeric A β 40 and CRANAD-2 was most likely weak. We reasoned that this weak interaction could be enhanced by replacing the two phenyl rings with pyridyls to introduce hydrogen bonding between the engaged A β fragment and the nitrogen atoms of the pyridines (48, 49). To this end, we designed CRANAD-3, which was synthesized by a procedure similar to that used for CRANAD-2 (Fig. 1 A and B); its structure was confirmed by ^1H , ^{13}C , and ^{19}F NMR/MS spectra (Fig. S1).

In Vitro Characterization of CRANAD-3. As expected, CRANAD-3 displayed an emission peak around 730 nm (Fig. 1C) in PBS and showed an excellent fluorescence response toward soluble species such as A β monomers, dimers, and oligomers (Fig. 2A). It displayed 12.3-, 39.5-, 16.3-, and 16.1-fold increases in fluorescence intensity at 670, 650, 670, and 650 nm for A β 40 monomers, A β 42 monomers, A β 42 dimers, and A β 42 oligomers, respectively. CRANAD-3 also showed a significant emission wavelength shift upon mixing with these soluble species (Fig. 2A). We found that CRANAD-3 exhibited strong binding with A β 40/42 monomers, dimers, and oligomers ($K_d = 24 \pm 5.7$ nM, 23 ± 1.6 nM, 16 ± 6.7 nM, and 27 ± 15.8 nM, respectively) (Fig. S2).

Because A β oligomers (A β O) have been considered the highly neurotoxic species in AD pathology (16–21), we conducted further comprehensive validation confirming that the fluorescence changes in CRANAD-3 originated from the interaction with A β O. First, we performed immunoprecipitation investigations with A β O-specific antibody A11 (50). We compared the fluorescence changes in two A β 42O solutions, A and B, before and after immunoprecipitation. Solution A, which contained CRANAD-3 and A β 42O, was used as control. In solution B, CRANAD-3, A β 42O, and A11 antibody were mixed. We observed a 92% decrease in fluorescence intensity in solution B after precipitation with magnetic beads but only a 26% decrease in the control solution A (Fig. S3 A and B). These data strongly indicated that A β 42O is the primary species contributing to the changes in fluorescence intensity. Second, we conducted titration experiments with CRANAD-3 and various

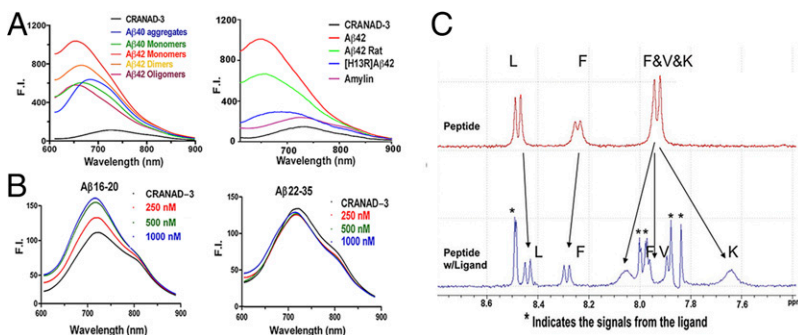


Fig. 2. Fluorescence spectra and NMR testing of CRANAD-3 with various A β s and fragments. (A) Fluorescence spectra of CRANAD-3 with soluble and insoluble A β s (Left) and with amylin, rat A β s, and mutated A β s (Right). (B) Fluorescence spectra of CRANAD-3 with core fragment A β 16–20 (KLVFF) (Left) and noncore fragment A β 22–35 (Right). (C) ^1H NMR spectra of KLVFF without (Upper) and with (Lower) CRANAD-3. Asterisks indicate peaks from CRANAD-3.

concentrations of A β 42O and achieved an excellent linear regression fit (Fig. S3 C and D). Third, we performed dot blotting for various concentrations of A β 42O with A11 antibody (Fig. S3 E and F) and examined the correlation between the fluorescence signal and the signal from dot blotting. An excellent correlation was achieved between the two groups of signals (Fig. S3G), indicating that the fluorescence intensity can be used to reflect the content of A β 42O. Moreover, we also conducted immunoprecipitation with fibril-specific OC antibody (51, 52) and observed a significant decrease in signal with A β 40 aggregates (Fig. S3H). As expected, no significant decrease was observed for A β 42O (Fig. S3I), indicating the absence of any significant amount of fibrillar A β s in the tested A β 42O solution. In addition, thioflavin-T testing, which is sensitive for insoluble fibrillar A β s but not soluble oligomers, confirmed that the majority of the tested A β 42O are nonfibrillar A β s (Fig. S3J). This result was validated further by dot blotting with OC antibody (Fig. S3K).

Studies showed that pyroglutamate A β [A β N3(pE)] contributed substantially to AD pathology because of its high neurotoxicity and abundance in AD brains (53, 54). To investigate whether CRANAD-3 can interact with A β N3(pE), we performed fluorescence spectral testing similar to experiments with other A β s. We found that the fluorescence intensity of CRANAD-3 increased significantly upon mixing with A β N3(pE) (Fig. S4A), indicating that CRANAD-3 is sensitive for A β N3(pE). In addition, CRANAD-3 displayed a significant increase in intensity and wavelength shift upon interaction with insoluble A β 40 aggregates (Fig. 2A), suggesting that CRANAD-3 can detect both insoluble and soluble A β s.

To investigate the specificity of CRANAD-3 for A β species, amylin [an aggregation-prone 37-residue peptide secreted together with insulin by pancreatic B cells (55)] was incubated with CRANAD-3. No significant fluorescence property changes were observed (Fig. 2A), suggesting CRANAD-3's excellent selectivity toward A β species. We also tested the interaction of CRANAD-3 with other amyloidogenic proteins, such as Tau 441 and α -synuclein, and observed no significant increase in fluorescence (Fig. S4B). In addition, we investigated the specificity of CRANAD-3 toward rat A β (the differences from human A β are R5G, Y10F, and H13R) and mutated (H13R) A β and found a significant decrease in fluorescence intensity (Fig. 2A), suggesting that these probes are highly specific toward human A β s.

We also investigated whether CRANAD-3 could interact with the core fragment KLVFF (A β 16–20) of A β s. In vitro tests showed that the fluorescence intensities increased with the concentrations of KLVFF fragment (Fig. 2B). This result was consistent with our ^1H NMR data, in which apparent changes in the chemical shift of amide protons were observed when CRANAD-3 was incubated with the fragment (Fig. 2C). Therefore, both fluorescence and NMR data suggested that CRANAD-3 interacts with the core fragment. In addition, no significant change in fluorescence property was observed when CRANAD-3 was mixed with a noncore fragment, A β 22–35 (Fig. 2B). We also investigated whether this interaction was sequence dependent. In this regard, we tested the changes in the fluorescence intensity of CRANAD-3 with KLVLL, in which two phenylalanines were replaced by hydrophobic leucine. No significant changes in intensity were found (Fig. S4C), indicating that the interaction is sequence dependent and that phenylalanine residues are critical for the binding. Although we believe that CRANAD-3 interactions with A β species are sequence specific, conformational dependency also is possible. However, this hypothesis needs a separate investigation, which would be outside of the scope of the present study.

Two-Photon Imaging of A β Deposits with CRANAD-3. As a brain-imaging probe, CRANAD-3 must meet several requirements that include proper lipophilicity (log P) and reasonable penetration of the brain–blood barrier (BBB) (47). We found that log P

for CRANAD-3 was 2.50, which is reasonable for brain imaging. To investigate whether CRANAD-3 is capable of penetrating the BBB, we used two-photon imaging to test its accumulation in the brain. Two-photon imaging is a microscopic technology that has been used widely for visualizing A β plaques in live mice (56, 57). As expected, two-photon images from transgenic AD mice indicated that CRANAD-3 is able to label A β plaques and cerebral amyloid angiopathies [CAAs, i.e., A β deposits at the exterior of brain blood vessels (58, 59)] (Fig. 3 A–C), suggesting that this probe can cross the BBB and specifically label A β species in vivo. In addition, the probe accumulated gradually in the brain and reached its peak around 10 min after injection, followed by a slow washout (Fig. 3D). Ex vivo histology confirmed that CRANAD-3 clearly labeled A β plaques in brain sections, further indicating its ability to penetrate the BBB (Fig. 3 E–H and Fig. S5) and its specificity for A β species. No apparent plaques were observed in the age-matched wild-type mice by two-photon imaging and ex vivo histology (Fig. 3C and Fig. S5).

In Vivo NIRF Imaging of APP/PS1 Transgenic Mice with CRANAD-3.

APP/PS1 mice, the most studied transgenic AD mouse model (24, 56), were used to test the utility of CRANAD-3 for in vivo NIRF imaging. This mouse model possesses double humanized APP/PS1 genes and constantly produces considerable amounts of “human” A β s. Previous studies indicate that APP/PS1 mice have no significant A β deposits or any noticeable behavioral abnormalities before 6 mo of age. It is believed that the majority of A β species in mice younger than 6 mo are soluble (24, 56). To test whether CRANAD-3 was able to detect soluble species in vivo by NIRF imaging, we used 4-mo-old APP/PS1 mice. We found that after i.v. injection the fluorescence signal from the brain of APP/PS1 mice was significantly higher than that from the age-matched wild-type mice at all time points used (Fig. 4). The signals from APP/PS1 mice were 2.29-, 2.04-, 1.98-, 1.60-, and 1.54-fold higher than the signals from wild-type controls at 5, 10, 30, 60, and 120 min after injection (Fig. 4),

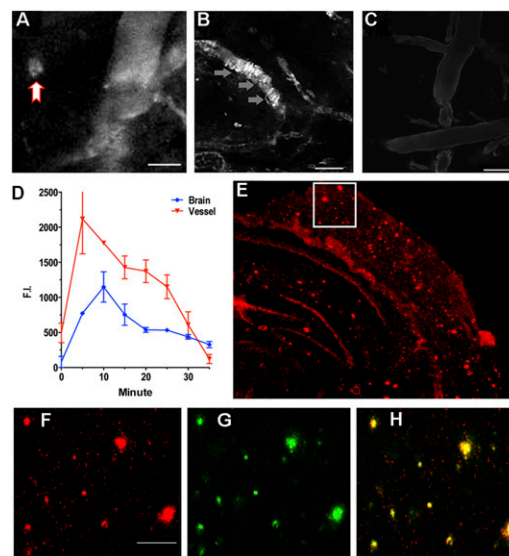


Fig. 3. (A–C) Representative two-photon microscopic images with CRANAD-3 in a 14-mo-old APP/PS1 mouse (A and B) and in a wild-type control mouse (C). The red arrow in A indicates plaque. The gray arrow in B indicates CAA labeling. (Scale bars: 100 μm .) (D) Quantitative analysis of fluorescence intensity in blood vessels and in brain. Five or six ROIs were averaged. (E) Ex vivo histology of a mouse brain slice obtained after the two-photon imaging with CRANAD-3. (F) Magnified image of the boxed area in E. (Scale bar: 50 μm .) (G) Thioflavin-S-costained image. (H) Merged image of F and G.

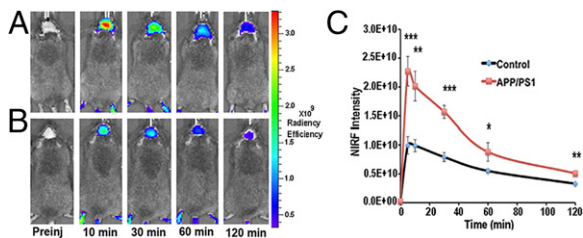


Fig. 4. Representative images of APP/PS1 and wild-type control mice at different time points before and after i.v. injection of 0.5 mg/kg of CRANAD-3. (A and B) Images from a 4-mo-old APP-PS1 mouse (A) and a 4-mo-old control mouse (B). (C) Quantitative analysis of fluorescence signals from transgenic APP/PS1 mice and control mice ($n = 3$ or 4) at preinjection and 5, 10, 30, 60, and 120 min after i.v. injection. The signals were significantly higher in 4-mo-old APP/PS1 mice than in the age-matched control mice. * $P < 0.05$, ** $P < 0.01$, *** $P < 0.005$.

suggesting that CRANAD-3 indeed is capable of detecting soluble A β species in vivo.

Proof-of-Concept Application of CRANAD-3 for Therapy Monitoring.

Our two-photon microscopic imaging and NIRF imaging indicated that CRANAD-3 is able to penetrate the BBB and is specific toward A β species. These results encouraged us to investigate CRANAD-3's capacity for monitoring therapy. To this end, we used two experimental drugs to conduct proof-of-concept experiments.

Monitoring the rapid A β -lowering effect of inhibiting beta-amyloid cleaving enzyme-1. Developing beta-amyloid cleaving enzyme-1 (BACE-1) inhibitors is one of the current mainstream approaches for AD drug discovery, and several drug candidates have advanced into clinical trials. Although none of the BACE-1 inhibitors is presently approved by the FDA for clinical use, several inhibitors show consistent efficacy in lowering soluble A β species in transgenic mice in a short period of treatment. Because our imaging probe can detect soluble A β s, we conducted NIRF imaging to investigate whether CRANAD-3 can monitor the rapid reduction of soluble A β s. We first tested the capacity of CRANAD-3 with the well-characterized BACE-1 inhibitor LY2811376, which could lead to a 60% decrease in the soluble A β s in mouse cortex after a single oral dose (30 mg/kg) (60). As expected, the fluorescence signal of CRANAD-3 from APP/PS1 mice ($n = 4$) after LY2811376 treatment was 33% lower than the signal from the same mice before treatment (Fig. 5A and B). The difference detected by our near-infrared (NIR) imaging was smaller than that reported from ELISA with brain extracts (33% vs. 60%), very likely because an A β antibody-based ELISA is more specific than our NIRF small molecule.

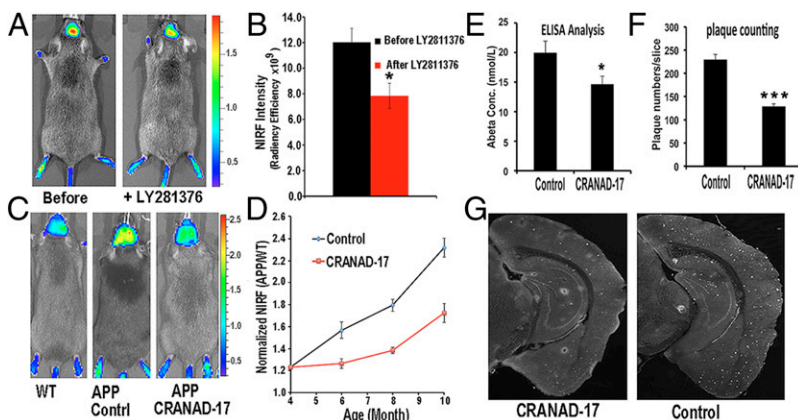


Fig. 5. Application of CRANAD-3 for monitoring therapeutic effects of drug treatments. (A) In vivo imaging of APP/PS1 mice with CRANAD-3 before and after treatment with the BACE-1 inhibitor LY2811376. (B) Quantitative analysis of the imaging in A ($n = 4$). (C) Representative images of 4-mo-old APP/PS1 mice after 6 mo of treatment with CRANAD-17. (Left) Age-matched WT mouse. (Center) Control APP/PS1 mouse. (Right) CRANAD-17-treated APP/PS1 mouse. Note that the NIRF signal from the CRANAD-17-treated APP/PS1 mouse (Right) is lower than the signal from the nontreated control APP/PS1 mouse (Center). (D) Quantitative analysis of the imaging in C ($n = 5$). (E) ELISA analysis of total A β 40 from brain extracts. (F) Analysis of plaque counting. (G) Representative histological staining with thioflavin S. (Left) CRANAD-17-treated mouse. (Right) Control. * $P < 0.05$, ** $P < 0.01$, *** $P < 0.005$.

Monitoring long-term therapy with CRANAD-17. In our previous studies, we designed the imidazole-containing curcumin analog CRANAD-17, which could compete specifically with the H13, H14 of A β peptides and lead to a reduction of copper-induced A β cross-linking in vitro (46). We performed a preliminary in vivo therapeutic treatment of 4-mo-old APP/PS1 mice with CRANAD-17 for 6 mo. We treated mice ($n = 5$) with an i.p. injection of CRANAD-17 (2 mg/kg) twice a week, and the control APP/PS1 group ($n = 5$) was injected with the same volume of saline. After a 6-mo treatment, NIRF imaging with CRANAD-3 indicated that the CRANAD-17-treated group showed significantly lower NIRF signals (25%) than the nontreated group (Fig. 5C and D). This result was consistent with the ELISA analysis showing a 36% reduction in A β 40 in the brain extracts (Fig. 5E). Our ELISA results were confirmed further by Meso Scale Discovery (MSD) analysis (Fig. S6A) (61–63). We also observed a 25% decrease in A β 42 in the CRANAD-17-treated group by MSD analysis, although the difference between the two groups did not reach statistical significance (Fig. S6B). In addition, our NIR imaging result was consistent with plaque counting in brain slices stained with thioflavin-S, which showed a 56% reduction with CRANAD-17 treatment (Fig. 5F and G). Interestingly, a comparison of the brain slices from the two groups showed that the number of dimly fluorescent and diffused plaques apparently was lower in the treated group than in the control group (Fig. 5G and Fig. S7), probably because of the anti-cross-linking capability of CRANAD-17.

Our data from both short and chronic treatment studies strongly suggest that CRANAD-3 could be used to monitor the therapeutic effectiveness of drug treatment. Further protocol optimization is ongoing in Ran's group.

Discussion

Fluorescence molecular imaging technologies have advanced very rapidly in the past decade, particularly for peripheral diseases such as cancer and cardiovascular disease. However, its development and applications for CNS diseases has progressed sluggishly. PET imaging has been used widely for CNS diseases; however, its applications in preclinical studies have been limited because of the use of radioisotopes, the short lifetime of the imaging probes, its high cost, and facility requirements. Fluorescence molecular imaging is appealing for small animal studies because of its low cost, easy operation, and stable imaging probes. In the past decade, the development of fluorescent imaging probes for AD has been actively pursued, and several probes showed capacity for imaging A β s (37–45) and Tau tangles (64) in mice. Nonetheless, none has been used to monitor the effectiveness of drug therapy.

Recent evidence shows that soluble A β s, such as dimers and oligomers, are more neurotoxic than insoluble deposits and thus

potentially could serve as biomarkers for presymptomatic stages of AD (2, 21). In the past decades, drug-development strategies using insoluble A β deposits as biomarkers for evaluation of AD have failed; this failure has led to a shift in research toward the targeting of soluble A β s and to more clinical trials being conducted at the early/presymptomatic stage of AD (14). Imaging probes capable of detecting soluble A β s are needed both for clinical trials and for preclinical evaluation.

Although both PET and NIRF probes for imaging A β s are available, they have a fundamental limitation: they primarily detect insoluble A β s, not the more toxic soluble A β s. In our previous studies, we designed and tested the NIRF probe CRANAD-58, a curcumin analog, for detecting both soluble and insoluble A β s (46). However, its sensitivity for in vivo imaging of A β s is lower than that of CRANAD-3 (the ratios of NIRF signal $F_{(APP/PS1)}/F_{(WT)}$ are 2.29 vs. 1.71, 2.04 vs. 1.61, and 1.98 vs. 1.82 at 5-, 10- and 30-min, respectively, after the probe injection) (46). Therefore, we decided to use CRANAD-3 to monitor therapeutic effectiveness in the proof-of-concept studies in this report.

The most remarkable advantage of CRANAD-3, compared with other NIRF imaging probes for A β s, is its ability to detect both soluble and insoluble A β s, making CRANAD-3 suitable for monitoring the rapid A β -lowering effect of BACE-1 inhibitors and other fast-acting drug candidates [i.e., bexarotene (63, 65–69) and citalopram (70)]. This ability is very important, because our imaging method would enable a quick evaluation of the efficacy of some categories of drug candidates, such as BACE-1 inhibitors, gamma-secretase inhibitors/modulators, and others (62, 71).

Our data indicate that CRANAD-3 is suitable for monitoring short-term and chronic treatments. However, more rigorous optimization is needed to make the protocol easily reproducible in other laboratories. Our optimization will focus on formulation, imaging procedure, and data analysis.

Two-photon microscopic imaging has been an important tool for studying amyloidosis of AD (57, 72–74). However, most of the fluorescent probes have short emission, which can limit imaging depth significantly. Although we did not intend to investigate the maximal imaging depth of CRANAD-3 in this report, we believe its NIR emission has the potential to enable deep two-photon imaging of A β plaques and CAAs.

Available transgenic AD models have different pathological features, with APP23, Tg2576, PSAPP (APPSwe/PS1M146L), and APP/PS1 mice being the models most often used (75, 76). Snellman et al. (77) recently reported that different mouse models have different retention capability for ^{11}C -PiB. Among the tested AD models, only APP23 mice showed substantial ^{11}C -PiB binding at the age of 18 mo. This result is consistent with data reported by Maeda et al. (78) and Mori et al. (79). Unlike previous PET imaging studies with PiB (30–32), these studies suggested that ^{11}C -PiB with highly specific radioactivity could be used for mouse imaging, particularly for APP23 mice. Both studies attributed the differences to pyroglutamate A β , which contributes significantly to the A β deposits in old APP23 mice and probably plays an important role in the plaque binding with

PiB (77–79). Our fluorescence data indicate that CRANAD-3 is responsive to pyroglutamate A β s, suggesting that it could be used as an imaging probe with other AD models such as APP23 mice.

In this report, we demonstrated that CRANAD-3 is capable of detecting soluble A β both in vitro and in vivo. We believe that CRANAD-3 may be a potential probe for monitoring β -amyloid species at an early/presymptomatic stage of AD. However, the present limitations of fluorescence imaging in human subjects are clearly major obstacles to the clinical use of CRANAD-3. Recently, at least two emerging technologies have shown considerable promise for overcoming the practical difficulties of using CRANAD-3 in humans. First, rapid advances in fluorescence molecular tomography indicate that suitable scanners with penetrating capabilities up to 10 cm may be readily available soon (80, 81). Second, it is likely that the incorporation of isotopes into CRANAD-3 molecules will facilitate the use of the probe for PET imaging, which is a widely used clinical modality. These studies are currently under way in the C.R. laboratory.

Materials and Methods

Reagents used for the synthesis of CRANAD-3 were purchased from Aldrich and were used without further purification. All animal experiments were performed in compliance with institutional guidelines and were approved by the Institutional Animal Care and Use Committee at the Massachusetts General Hospital.

Full descriptions of methods used are available in *SI Materials and Methods*.

Testing of CRANAD-3 with A β 40/42 Monomers, A β 42 Dimers, A β 42 Oligomers, and A β 40 Aggregates. To test interactions of CRANAD-3 with A β species, we use the following three-step procedure. In step 1, 1.0 mL of double-distilled water was added to a quartz cuvette as a blank control, and its fluorescence was recorded with the same parameters as for CRANAD-3. In step 2, fluorescence of a CRANAD-3 solution (1.0 mL, 250 nM) was recorded with excitation at 580 nm and emission from 610–900 nm. In step 3, to the above CRANAD-3 solution, 10 μL of A β species [25- μM stock solution in 30% (vol/vol) trifluoroethanol or hexafluoroisopropanol (HFIP) for monomers and dimers and 25- μM stock solution in PBS buffer for A β 40 aggregates] was added to make the final A β concentration 250 nM. Fluorescence readings from this solution were recorded as described in step 2. A blank control from step 1 was used to correct the final spectra from steps 2 and 3.

In Vivo NIRF Imaging. The IVIS Spectrum animal imaging system (PerkinElmer) was used to perform In vivo NIR imaging. Images were acquired with a 605-nm excitation filter and a 680-nm emission filter. Living Image 4.2 software (PerkinElmer) was used for data analysis.

Mice ($n = 3$ or 4 female transgenic APP-PS1 mice and $n = 3$ or 4 age-matched female wild-type control mice) were shaved before background imaging and were i.v. injected with freshly prepared CRANAD-3 [0.5 mg/kg, 15% (vol/vol) DMSO, 15% (vol/vol) cremophor, and 70% (vol/vol) PBS]. Fluorescence signals from the brain were recorded before and 5, 10, 30, 60, 120, and 180 min after i.v. injection of the probe. To evaluate our imaging results, a region of interest (ROI) was drawn around the brain region. Student t-test was used to calculate P values.

ACKNOWLEDGMENTS. We thank Pamela Pantazopoulos for proofreading the manuscript. This work was supported by Award K25AG036760 from NIH (to C.R.).

- Giacobini E, Gold G (2013) Alzheimer disease therapy—moving from amyloid- β to tau. *Nat Rev Neurol* 9(12):677–686.
- Selkoe DJ (2011) Resolving controversies on the path to Alzheimer's therapeutics. *Nat Med* 17(9):1060–1065.
- Abbott A (2008) Neuroscience: The plaque plan. *Nature* 456(7219):161–164.
- Buckholtz NS, Ryan LM, Petanceska S, Refolo LM (2012) NIA commentary: Translational issues in Alzheimer's disease drug development. *Neuropsychopharmacology* 37(1):284–286.
- Jonsson T, et al. (2012) A mutation in APP protects against Alzheimer's disease and age-related cognitive decline. *Nature* 488(7409):96–99.
- Castellani RJ, et al. (2009) Reexamining Alzheimer's disease: Evidence for a protective role for amyloid-beta protein precursor and amyloid-beta. *J Alzheimers Dis* 18(2):447–452.
- Kim T, et al. (2013) Human LirB2 is a β -amyloid receptor and its murine homolog PirB regulates synaptic plasticity in an Alzheimer's model. *Science* 341(6152):1399–1404.
- John V, ed (2010) *BACE: Lead Target for Orchestrated Therapy of Alzheimer's Disease* (Wiley, Hoboken, NJ).
- Faux NG, et al. (2010) PBT2 rapidly improves cognition in Alzheimer's Disease: Additional phase II analyses. *J Alzheimers Dis* 20(2):509–516.
- Monceaux CJ, et al. (2011) Triazole-linked reduced amide isosteres: An approach for the fragment-based drug discovery of anti-Alzheimer's BACE1 inhibitors. *Bioorg Med Chem Lett* 21(13):3992–3996.
- Lee J, et al. (2011) Identification of presenilin 1-selective γ -secretase inhibitors with reconstituted γ -secretase complexes. *Biochemistry* 50(22):4973–4980.
- Barrow JC, et al. (2008) Discovery and X-ray crystallographic analysis of a spiro-piperidine iminohydantoin inhibitor of beta-secretase. *J Med Chem* 51(20):6259–6262.
- Zhang MR, et al. (2005) Synthesis and evaluation of N-(5-fluoro-2-phenoxyphenyl)-N-(2-[(18)F]fluoromethoxy-d(2)-5-methoxybenzyl)acetamide: A deuterium-substituted radioligand for peripheral benzodiazepine receptor. *Bioorg Med Chem* 13(5):1811–1818.

14. Sperling RA, et al. (2014) The A4 study: Stopping AD before symptoms begin? *Sci Transl Med* 6(228):228fs13.
15. Choi SH, et al. (2014) A three-dimensional human neural cell culture model of Alzheimer's disease. *Nature* 515(7526):274–278.
16. McLean CA, et al. (1999) Soluble pool of Abeta amyloid as a determinant of severity of neurodegeneration in Alzheimer's disease. *Ann Neurol* 46(6):860–866.
17. Lue LF, et al. (1999) Soluble amyloid beta peptide concentration as a predictor of synaptic change in Alzheimer's disease. *Am J Pathol* 155(3):853–862.
18. Terry RD, et al. (1991) Physical basis of cognitive alterations in Alzheimer's disease: Synapse loss is the major correlate of cognitive impairment. *Ann Neurol* 30(4):572–580.
19. Townsend M, Mehta T, Selkoe DJ (2007) Soluble Abeta inhibits specific signal transduction cascades common to the insulin receptor pathway. *J Biol Chem* 282(46):33305–33312.
20. Walsh DM, Selkoe DJ (2007) A beta oligomers - a decade of discovery. *J Neurochem* 101(5):1172–1184.
21. Shankar GM, et al. (2008) Amyloid-beta protein dimers isolated directly from Alzheimer's brains impair synaptic plasticity and memory. *Nat Med* 14(8):837–842.
22. Hardy J, Selkoe DJ (2002) The amyloid hypothesis of Alzheimer's disease: Progress and problems on the road to therapeutics. *Science* 297(5580):353–356.
23. Mawuenyega KG, et al. (2010) Decreased clearance of CNS beta-amyloid in Alzheimer's disease. *Science* 330(6012):1774–1776.
24. Hsiao K, et al. (1996) Correlative memory deficits, Abeta elevation, and amyloid plaques in transgenic mice. *Science* 274(5284):99–102.
25. Cao D, Lu H, Lewis TL, Li L (2007) Intake of sucrose-sweetened water induces insulin resistance and exacerbates memory deficits and amyloidosis in a transgenic mouse model of Alzheimer disease. *J Biol Chem* 282(50):36275–36282.
26. Kantarci K, et al. (2012) Antemortem amyloid imaging and β -amyloid pathology in a case with dementia with Lewy bodies. *Neurobiol Aging* 33(5):878–885.
27. Ikonomic MD, et al. (2008) Post-mortem correlates of in vivo PiB-PET amyloid imaging in a typical case of Alzheimer's disease. *Brain* 131(Pt 6):1630–1645.
28. Kalaitzakis ME, Pearce RK (2013) Beyond the limits of detection: Failure of PiB imaging to capture true A β burden. *Mov Disord* 28(3):406.
29. Gomperts SN, Johnson KA, Growdon J (2013) Reply: Beyond the limits of detection: Failure of PiB imaging to capture true A β burden. *Mov Disord* 28(3):407.
30. Mathis CA, Mason NS, Lopresti BJ, Klunk WE (2012) Development of positron emission tomography β -amyloid plaque imaging agents. *Semin Nucl Med* 42(6):423–432.
31. Zhang L, Chang RC, Chu LW, Mak HK (2012) Current neuroimaging techniques in Alzheimer's disease and applications in animal models. *Am J Nucl Med Mol Imaging* 2(3):386–404.
32. Kuntner C, et al. (2009) Limitations of small animal PET imaging with ^{18}F FDNP and FDG for quantitative studies in a transgenic mouse model of Alzheimer's disease. *Mol Imaging Biol* 11(4):236–240.
33. Nordberg A (2011) Molecular imaging in Alzheimer's disease: New perspectives on biomarkers for early diagnosis and drug development. *Alzheimers Res Ther* 3(6):34.
34. Jack CR, Jr, et al. (2004) In vivo visualization of Alzheimer's amyloid plaques by magnetic resonance imaging in transgenic mice without a contrast agent. *Magn Reson Med* 52(6):1263–1271.
35. Klunk WE, et al. (2004) Imaging brain amyloid in Alzheimer's disease with Pittsburgh Compound-B. *Ann Neurol* 55(3):306–319.
36. Nordberg A, Rinne JO, Kadir A, Långström B (2010) The use of PET in Alzheimer disease. *Nat Rev Neurol* 6(2):78–87.
37. Jakob-Roetne R, Jacobsen H (2009) Alzheimer's disease: From pathology to therapeutic approaches. *Angew Chem Int Ed Engl* 48(17):3030–3059.
38. Chang WM, et al. (2011) ANCA: A family of fluorescent probes that bind and stain amyloid plaques in human tissue. *ACS Chem Neurosci* 2(5):249–255.
39. Choi SR, et al. (2009) Preclinical properties of ^{18}F -AV-45: A PET agent for Abeta plaques in the brain. *J Nucl Med* 50(11):1887–1894.
40. Li Q, et al. (2004) Solid-phase synthesis of styryl dyes and their application as amyloid sensors. *Angew Chem Int Ed Engl* 43(46):6331–6335.
41. Hintersteiner M, et al. (2005) In vivo detection of amyloid-beta deposits by near-infrared imaging using an oxazine-derivative probe. *Nat Biotechnol* 23(5):577–583.
42. Cui M, Ono M, Kimura H, Liu B, Saji H (2011) Synthesis and structure-affinity relationships of novel dibenzylideneacetone derivatives as probes for β -amyloid plaques. *J Med Chem* 54(7):2225–2240.
43. Cui M, et al. (2014) Smart near-infrared fluorescence probes with donor-acceptor structure for in vivo detection of β -amyloid deposits. *J Am Chem Soc* 136(9):3388–3394.
44. Ono M, Watanabe H, Kimura H, Saji H (2012) BODIPY-based molecular probe for imaging of cerebral β -amyloid plaques. *ACS Chem Neurosci* 3(4):319–324.
45. Ran C, Zhao W, Moir RD, Moore A (2011) Non-conjugated small molecule FRET for differentiating monomers from higher molecular weight amyloid beta species. *PLoS One* 6(4):e19362.
46. Zhang X, et al. (2013) Design and synthesis of curcumin analogues for in vivo fluorescence imaging and inhibiting copper-induced cross-linking of amyloid beta species in Alzheimer's disease. *J Am Chem Soc* 135(44):16397–16409.
47. Ran C, et al. (2009) Design, synthesis, and testing of difluoroboron-derivatized curcumins as near-infrared probes for in vivo detection of amyloid-beta deposits. *J Am Chem Soc* 131(42):15257–15261.
48. Hanyu M, et al. (2005) Studies on intramolecular hydrogen bonding between the pyridine nitrogen and the amide hydrogen of the peptide: Synthesis and conformational analysis of tripeptides containing novel amino acids with a pyridine ring. *J Pept Sci* 11(8):491–498.
49. Rzepecki P, Schrader T (2005) beta-Sheet ligands in action: KLVFF recognition by aminopyrazole hybrid receptors in water. *J Am Chem Soc* 127(9):3016–3025.
50. Kaye R, et al. (2003) Common structure of soluble amyloid oligomers implies common mechanism of pathogenesis. *Science* 300(5618):486–489.
51. Wu JW, et al. (2010) Fibrillar oligomers nucleate the oligomerization of monomeric amyloid beta but do not seed fibril formation. *J Biol Chem* 285(9):6071–6079.
52. Kaye R, et al. (2007) Fibril specific, conformation dependent antibodies recognize a generic epitope common to amyloid fibrils and fibrillar oligomers that is absent in prefibrillar oligomers. *Mol Neurodegener* 2:18.
53. Schilling S, et al. (2006) On the seeding and oligomerization of pGlu-amyloid peptides (in vitro). *Biochemistry* 45(41):12393–12399.
54. Mori H, Takio K, Ogawara M, Selkoe DJ (1992) Mass spectrometry of purified amyloid beta protein in Alzheimer's disease. *J Biol Chem* 267(24):17082–17086.
55. Marshall KE, Serpell LC (2009) Structural integrity of beta-sheet assembly. *Biochem Soc Trans* 37(Pt 4):671–676.
56. Garcia-Alloza M, et al. (2006) Characterization of amyloid deposition in the APPsw/PS1dE9 mouse model of Alzheimer disease. *Neurobiol Dis* 24(3):516–524.
57. Zhang X, et al. (2014) A bifunctional curcumin analogue for two-photon imaging and inhibiting crosslinking of amyloid beta in Alzheimer's disease. *Chem Commun (Camb)* 50(78):11550–11553.
58. Smith EE, Greenberg SM (2009) Beta-amyloid, blood vessels, and brain function. *Stroke* 40(7):2601–2606.
59. de la Torre JC (2004) Is Alzheimer's disease a neurodegenerative or a vascular disorder? Data, dogma, and dialectics. *Lancet Neurol* 3(3):184–190.
60. May PC, et al. (2011) Robust central reduction of amyloid- β in humans with an orally available, non-peptidic β -secretase inhibitor. *J Neurosci* 31(46):16507–16516.
61. Zhang C, Browne A, Child D, Tanzi RE (2010) Curcumin decreases amyloid-beta peptide levels by attenuating the maturation of amyloid-beta precursor protein. *J Biol Chem* 285(37):28472–28480.
62. Wagner SL, et al. (2014) Soluble γ -secretase modulators selectively inhibit the production of the 42-amino acid amyloid β peptide variant and augment the production of multiple carboxy-truncated amyloid β species. *Biochemistry* 53(4):702–713.
63. Veeraghavalu K, et al. (2013) Comment on "ApoE-directed therapeutics rapidly clear beta-amyloid and reverse deficits in AD mouse models". *Science* 340(6135):924-f.
64. Maruyama M, et al. (2013) Imaging of tau pathology in a tauopathy mouse model and in Alzheimer patients compared to normal controls. *Neuron* 79(6):1094–1108.
65. Landreth GE, et al. (2013) Response to comments on "ApoE-directed therapeutics rapidly clear beta-amyloid and reverse deficits in AD mouse models". *Science* 340(6135):924-g.
66. Tessier I, et al. (2013) Comment on "ApoE-directed therapeutics rapidly clear beta-amyloid and reverse deficits in AD mouse models". *Science* 340(6135):924-e.
67. Price AR, et al. (2013) Comment on "ApoE-directed therapeutics rapidly clear beta-amyloid and reverse deficits in AD mouse models". *Science* 340(6135):924-d.
68. Fitz NF, Cronican AA, Lefterov I, Koldamova R (2013) Comment on "ApoE-directed therapeutics rapidly clear β -amyloid and reverse deficits in AD mouse models". *Science* 340(6135):924-c.
69. Cramer PE, et al. (2012) ApoE-directed therapeutics rapidly clear β -amyloid and reverse deficits in AD mouse models. *Science* 335(6075):1503–1506.
70. Sheline YI, et al. (2014) An antidepressant decreases CSF A β production in healthy individuals and in transgenic AD mice. *Sci Transl Med* 6(236):236re4.
71. Kounnas MZ, et al. (2010) Modulation of gamma-secretase reduces beta-amyloid deposition in a transgenic mouse model of Alzheimer's disease. *Neuron* 67(5):769–780.
72. Backskai BJ, et al. (2003) Four-dimensional multiphoton imaging of brain entry, amyloid binding, and clearance of an amyloid-beta ligand in transgenic mice. *Proc Natl Acad Sci USA* 100(21):12462–12467.
73. Nesterov EE, et al. (2005) In vivo optical imaging of amyloid aggregates in brain: Design of fluorescent markers. *Angew Chem Int Ed Engl* 44(34):5452–5456.
74. Grutzendler J, Yang G, Pan F, Parkhurst CN, Gan WB (2011) Transcranial two-photon imaging of the living mouse brain. *Cold Spring Harb Protoc* 2011(9):pdb.prot065474.
75. Ashe KH, Zahs KR (2010) Probing the biology of Alzheimer's disease in mice. *Neuron* 66(5):631–645.
76. Howlett DR (2011) APP transgenic mice and their application to drug discovery. *Histol Histopathol* 26(12):1611–1632.
77. Snellman A, et al. (2013) Longitudinal amyloid imaging in mouse brain with ^{11}C -PiB: Comparison of APP23, Tg2576, and APPsw-PS1dE9 mouse models of Alzheimer disease. *J Nucl Med* 54(8):1434–1441.
78. Maeda J, et al. (2007) Longitudinal, quantitative assessment of amyloid, neuroinflammation, and anti-amyloid treatment in a living mouse model of Alzheimer's disease enabled by positron emission tomography. *J Neurosci* 27(41):10957–10968.
79. Mori T, et al. (2012) Molecular imaging of dementia. *Psychogeriatrics* 12(2):106–114.
80. Weissleder R, Pittet MJ (2008) Imaging in the era of molecular oncology. *Nature* 452(7187):580–589.
81. Luker GD, Luker KE (2008) Optical imaging: Current applications and future directions. *J Nucl Med* 49(1):1–4.
82. Moir RD, et al. (2005) Autoantibodies to redox-modified oligomeric Abeta are attenuated in the plasma of Alzheimer's disease patients. *J Biol Chem* 280(17):17458–17463.
83. Mostany R, Portera-Cailliau C (2008) A craniotomy surgery procedure for chronic brain imaging. *J Vis Exp* (12):pii680.
84. Borchelt DR, et al. (1996) Familial Alzheimer's disease-linked presenilin 1 variants elevate Abeta1-42/1-40 ratio in vitro and in vivo. *Neuron* 17(5):1005–1013.